

A compact sub-Kelvin ultrahigh vacuum scanning tunneling microscope with high energy resolution and high stability

L. Zhang, T. Miyamachi, T. Tomanić, R. Dehm, and W. Wulfhekel

Citation: *Rev. Sci. Instrum.* **82**, 103702 (2011); doi: 10.1063/1.3646468

View online: <http://dx.doi.org/10.1063/1.3646468>

View Table of Contents: <http://rsi.aip.org/resource/1/RSINAK/v82/i10>

Published by the [American Institute of Physics](#).

Related Articles

Hard x-ray scanning microscopy with coherent radiation: Beyond the resolution of conventional x-ray microscopes

Appl. Phys. Lett. **100**, 253112 (2012)

Design and analysis of multi-color confocal microscopy with a wavelength scanning detector

Rev. Sci. Instrum. **83**, 053704 (2012)

Wavefront corrected light sheet microscopy in turbid media

Appl. Phys. Lett. **100**, 191108 (2012)

Channelling optics for high quality imaging of sensory hair

Rev. Sci. Instrum. **83**, 045001 (2012)

Total internal reflection fluorescence microscopy imaging-guided confocal single-molecule fluorescence spectroscopy

Rev. Sci. Instrum. **83**, 013110 (2012)

Additional information on *Rev. Sci. Instrum.*

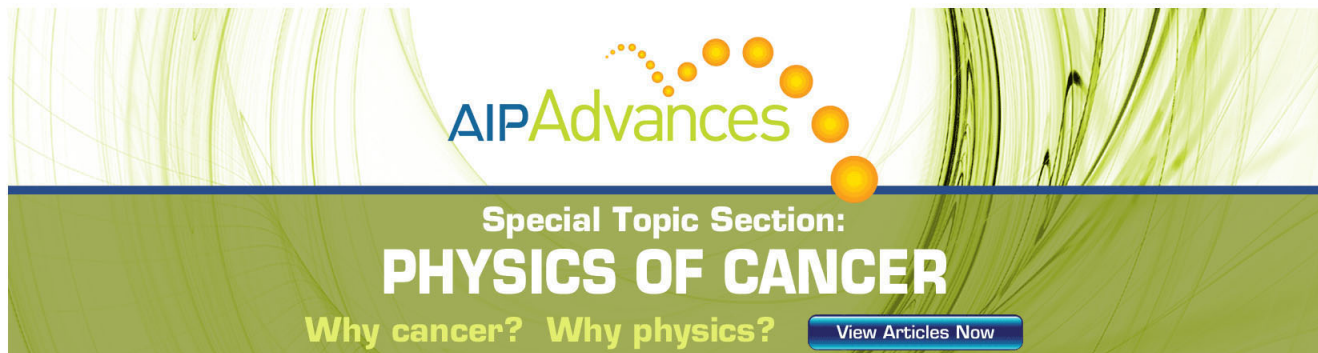
Journal Homepage: <http://rsi.aip.org>

Journal Information: http://rsi.aip.org/about/about_the_journal

Top downloads: http://rsi.aip.org/features/most_downloaded

Information for Authors: <http://rsi.aip.org/authors>

ADVERTISEMENT



AIP Advances

Special Topic Section:
PHYSICS OF CANCER

Why cancer? Why physics? [View Articles Now](#)

A compact sub-Kelvin ultrahigh vacuum scanning tunneling microscope with high energy resolution and high stability

L. Zhang, T. Miyamachi, T. Tomanić, R. Dehm, and W. Wulfhekel
 Physikalisches Institut, Karlsruhe Institute of Technology, Wolfgang-Gaede-Strasse 1,
 76131 Karlsruhe, Germany

(Received 23 February 2011; accepted 11 September 2011; published online 6 October 2011)

We designed a scanning tunneling microscope working at sub-Kelvin temperatures in ultrahigh vacuum (UHV) in order to study the magnetic properties on the nanoscale. An entirely homebuilt three-stage cryostat is used to cool down the microscope head. The first stage is cooled with liquid nitrogen, the second stage with liquid ^4He . The third stage uses a closed-cycle Joule-Thomson refrigerator of a cooling power of 1 mW. A base temperature of 930 mK at the microscope head was achieved using expansion of ^4He , which can be reduced to ≈ 400 mK when using ^3He . The cryostat has a low liquid helium consumption of only 38 ml/h and standing times of up to 280 h. The fast cooling down of the samples (3 h) guarantees high sample throughput. Test experiments with a superconducting tip show a high energy resolution of 0.3 meV when performing scanning tunneling spectroscopy. The vertical stability of the tunnel junction is well below 1 pm (peak to peak) and the electric noise floor of tunneling current is about $6\text{fA}/\sqrt{\text{Hz}}$. Atomic resolution with a tunneling current of 1 pA and 1 mV was achieved on Au(111). The lateral drift of the microscope at stable temperature is below 20 pm/h. A superconducting spilt-coil magnet allows to apply an out-of-plane magnetic field of up to 3 T at the sample surface. The flux vortices of a Nb(110) sample were clearly resolved in a map of differential conductance at 1.1 K and a magnetic field of 0.21 T. The setup is designed for *in situ* preparation of tip and samples under UHV condition. © 2011 American Institute of Physics. [doi:10.1063/1.3646468]

I. INTRODUCTION

For the study of nanoscopic structures, an instrument with high lateral resolution and high energy resolution for electronic states is needed. A usual solution for this requirement is a scanning tunneling microscope (STM) (Refs. 1–3) working at cryogenic temperatures.^{4–11} For surface science studies of atomically clean structures, the STM needs to be operated in ultrahigh vacuum (UHV).^{3,12–14} Typical commercially available low temperature STMs working in UHV use normally He-bath cryostat and operate at ≥ 4.2 K.^{15–17} The energy resolution of inelastic scanning tunneling spectroscopy (ISTS) at the temperature T is limited to $5.4 k_B T$ (Ref. 18) which is only about 1.9 meV at 4.2 K. For many interesting questions such as the study of magnetic excitations of single atoms and molecules,^{19–21} this resolution is insufficient and lower temperatures are required. For many studies on these magnetic nanostructures, the use of magnetic tips is advantageous,²² requiring frequent tip preparation with easy tip exchange entirely in UHV. To meet all these requirements, an ultra stable and low noise STM operating at 400 mK using ^3He (930 mK using ^4He) has been developed.

II. SYSTEM DESIGN

Figure 1 shows the overall design of the UHV recipient including the cryostat chamber (1) and the preparation chamber (2). The overall height is kept low to allow assembly and operation of the set up in rooms of only 3 m height. The microscope head (6) is placed inside the cryostat chamber, while tip and sample preparation are carried out in the preparation chamber. The two chambers are separated by an

UHV valve to avoid argon adsorption during ion sputtering. Using a molecular beam evaporator which is facing the STM head (6), *in situ* deposition of single atoms or molecules is possible without increasing the sample temperature above 12 K. Through subsequent cooling, the sample reaches the base-temperature within 10 min after the deposition procedure. The preparation chamber is equipped with an ion sputter-gun, allowing Ar^+ ion etching, several molecular beam evaporators, a quadrupole mass spectrometer, and an homebuilt electron bombardment heater for tips and samples with $T_{\text{max}} > 1500$ K. For surface analysis, a combined low energy electron diffractometer (LEED) and an Auger electron spectroscopy are installed. Further, the preparation chamber is connected to a load lock for quick sample and tip transfer into and out of vacuum without disturbing the UHV in the main chamber.

To maintain the UHV, both chambers are continuously pumped by ion getter pumps. After baking the preparation chamber at 250 °C and the cryostat chamber at ≈ 150 °C, a base-pressure of $< 2 \times 10^{-10}$ mbar was reached.

A. Cryostat

The development of the compact cryostat was the main part of the project. The overall aim was to achieve sub-Kelvin temperatures at the microscope head even without using expensive ^3He . To minimize the consumption of liquid He and liquid N_2 , the input heating power on the cryogenic baths must be as low as possible. For quick sample and tip exchange, easy access to the microscope head and good thermal conductivity between the microscope head and the cryostat

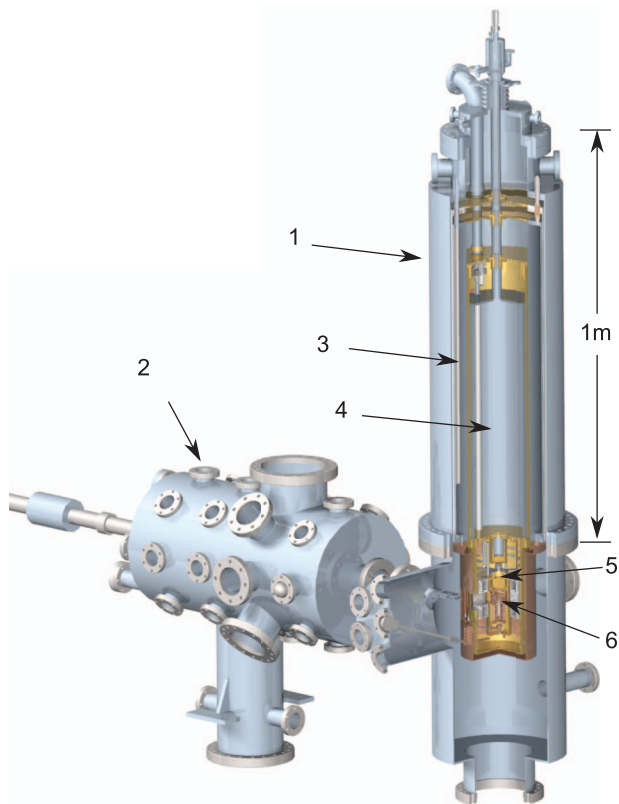


FIG. 1. (Color online) Layout of the UHV recipient with (1) the cryostat chamber, (2) the preparation chamber, (3) liquid nitrogen bath cryostat, (4) liquid helium bath cryostat, (5) Joule-Thomson cryostat, and (6) microscope head.

are both necessary. Furthermore, the microscope head must be isolated from the mechanical vibration from the cryogenic liquids. To achieve UHV conditions, it is indispensable that the system can be baked out at high temperatures. For all of these requirements, a homebuilt cryostat using the Joule-Thomson effect was developed.

Figure 2 shows a scheme of the cryostat with a total height of 120 cm and a diameter of 30 cm consisting of three cooling stages. The first and the second stage are concentric bath cryostats containing 20 l liquid N_2 (1) and 10 l liquid 4He (2), respectively. All of the containers of the cryogenic liquids are radiation shielded (6) so that the input thermal power remains low. The shields themselves are of high thermal conductivity (oxygen free copper) coated with a highly reflective material (silver or gold) to minimize the impact of heat radiation. Moreover, the shields around the nitrogen and helium baths are thermally coupled to the exhausting cryogenic gas via heat exchangers (7). Therefore, the heat capacity of the cold gas is used to further cool the radiation shields. As the main source of heat input on the cold bath is given by thermal radiation, which scales with T^4 , even a small decrease of the temperature of the shields substantially lowers the consumption of the cryogenic liquids.

The last cooling stage consists of a 3He Joule-Thomson cooler. Its working principle is shown in Fig. 3. 3He gas is injected into the cryostat at room temperature and at $p > 1.5$ bar and subsequently pre-cooled in a first concentric counter-current heat exchanger mounted inside the 3He pumping

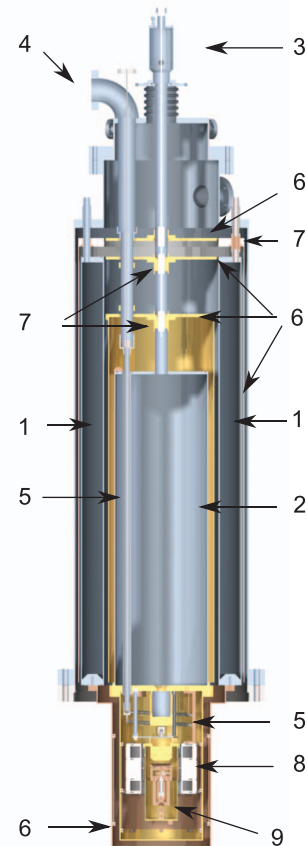


FIG. 2. (Color online) Scheme of the cryostat. (1) Liquid nitrogen tank, (2) liquid helium tank, (3) in and out let of liquid helium, (4) in and out let of 3He , (5) countercurrent heat exchanger for 3He , (6) radiation shield, (7) heat exchangers coupled with cryogenic gas, (8) superconductive coil, and (9) microscope head.

line. To prevent impurities in the 3He gas that could block the Joule-Thomson expansion capillary, a filter with a volume of ≈ 1.3 cm 3 , which is thermally anchored to the cooled radiation shield at ≈ 40 K, was inserted into the first heat exchanger. In a next step, the 3He is cooled down to 4.2 K within a 1-m long pipe, which is thermally anchored to the bottom of the liquid helium bath cryostat. This is followed by a second countercurrent heat exchanger consisting of a 10 m spiral encapsulated in the pumping line. Finally, the gas can freely expand through a capillary with a diameter of 90 μ m, thereby reaching sub-kelvin temperatures due to the Joule-Thomson effect. A reservoir of 10 ml is placed at the end of the capillary, which is pumped by an external pump to a pressure of ≈ 0.1 mbar. The total throughput of 3He gas in steady state corresponds to 3 l gas per hour under ambient conditions

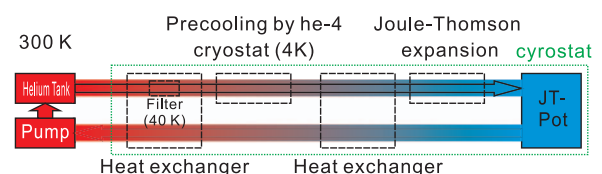


FIG. 3. (Color online) Schematics of the 3He cycle in Joule-Thomson cooling stage.

giving an estimated cooling power of 1 mW at 500 mK.²³ Below the Joule-Thomson cryostat, the cryogenic STM is mounted. It is vibrationally insulated from the Joule-Thomson stage by three springs and is thermally anchored to the Joule-Thomson stage by thin Au wires (50 μm). The input of heat is kept at a minimum ($<100 \mu\text{W}$) by thermal insulation of the ^3He stage from the ^4He cooled parts of the cryostat. This enables to use the ^3He bath also in the single shot mode. To avoid excessive warming during sample transfer, the warm sample is pre-cooled on a pre-cooling station attached to the radiation shield of the liquid nitrogen bath cryostat at a temperature of 77 K. As the ^3He stage is well insulated from the ^4He stage, cooling down of new samples and tips would be very slow. Thus, after inserting a sample good thermal coupling between microscope head and liquid helium bath cryostat is required. To overcome this dilemma, a mechanical thermal switch, which can be easily controlled from the outside, was integrated. By using this switch, it only takes three hours to cool down a sample and a tip from room temperature to sub-Kelvin temperatures ensuring both quick tip and sample exchange and sub-Kelvin operation.

The performance of the cryostat was modeled by linear heat transport equations taking heat flows due to radiation, heat conduction, and the heat exchangers into considerations. As a good approximation, it was assumed that the containers of cryogenic liquids have a homogeneous temperature distribution as well as the radiation shields which were made of either aluminum or copper. The heat conduction inside cryogenic liquids and exhausting cryogenic gas was neglected. In this case, only the contribution of heat conduction between exhausting cryogenic gas and heat exchangers, and inside the pipes as in and out let of cryogenic liquids, were considered. The emissivity of polished metal surface at a wavelength of about 10 μm (corresponds to room temperature) was taken to calculate radiative heat transfer between parts with different temperatures.²⁴ Then the efficiency of heat exchangers was treated as free parameters in the model. They were later estimated by fitting the model with the experimental consumption of cryogenic liquids.

Then, the system was manufactured, assembled, and tested. Due to the lack of ^3He on the international market, the Joule-Thomson stage was operated with ^4He instead of ^3He . The careful design of the cryostat minimizes the input heat power to 8.5 W to the 77 K bath and 26.5 mW to the 4.2 K bath, so that the consumption of only 153 g/h of liquid N_2 and 4.7 g/h of liquid ^4He was achieved. This corresponds to standing times of 105 h for liquid nitrogen (20 l) and 280 h for liquid helium (10 l). Keeping in mind that the cryostat has to absorb the heat input of the ^3He injection and pumping lines (contributing $\approx 50\%$ of the total heat load on the 4.2 K bath) as well as of that of the 50 A current lines for the superconducting magnet, this consumption is extraordinary low. It could only be achieved by the design of highly efficient heat exchangers ($\approx 90\%$ efficiency for the nitrogen and $\approx 70\%$ for the helium) that use the heat capacity of the cold exhausting gas.

A calibrated Cernox cryogenic temperature sensor²⁵ was mounted on the Joule-Thomson stage and the microscope head to measure the temperature. In test experiments of the

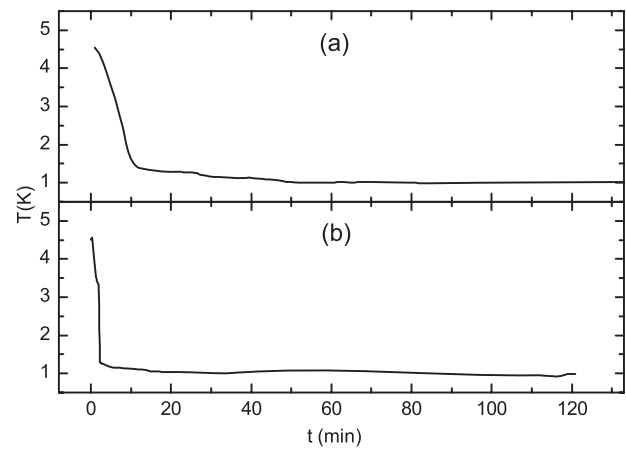


FIG. 4. Temperature of (a) the STM head and (b) the Joule-Thomson cryostat as a function of time after starting the Joule-Thomson expansion of ^4He .

Joule-Thomson expansion using ^4He , the cryostat cooled from 4.5 K to below 1 K in less than 20 min (see Fig. 4(b)). Similarly, the STM quickly cooled down to about 1.1 K during filling the Joule-Thomson cryostat in the first 20 min, which indicates an effective thermal coupling. After stopping the He input, a base temperature of 930 mK was reached until all the ^4He has been consumed (see Fig. 4(a)). In case the cavity of 10 ml in the last stage of the cryostat was completely filled with liquid ^4He and the Joule-Thomson expansion was stopped, standing times of the order of 20 h at the base temperature could be achieved with an operating STM indicating the low heat input on the sub-Kelvin components of the setup.

Because the vapor pressure above the helium surface depends mainly on the pumping speed of the Joule-Thomson exhaust system, it is reasonable to assume that the vapor pressure inside the Joule-Thomson cryostat is essentially independent on the isotope of He used. Considering the helium vapor pressure as one of the most common scales of low temperatures,^{26,27} the base temperature of 930 mK for ^4He converts to an expected base temperature of 420 mK when being operated with ^3He .

In the latest test the Joule-Thomson stage of the cryostat was operated using a mixture of 0.5 g ^3He and 0.6 g ^4He instead of pure ^4He . A compact homebuilt ^3He handling system was manufactured to pumping, storing and purifying the ^3He - ^4He mixture. With a slower cooling process (see Fig. 5) comparing to using pure ^4He , a temperature of 690 mK at the STM head was achieved. Even lower temperatures and a

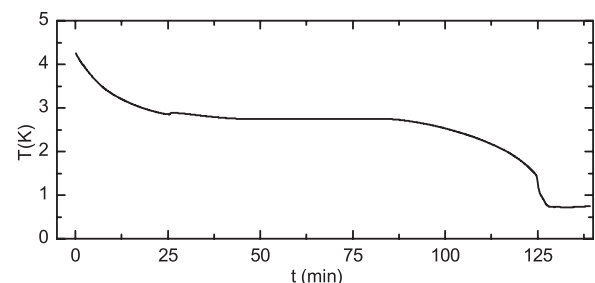


FIG. 5. Temperature of the STM head as a function of time after starting the Joule-Thomson expansion of ^3He - ^4He mixture.

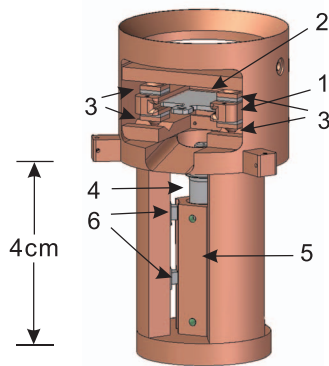


FIG. 6. (Color online) Schematics of STM head, (1) sample rack, (2) sample and sample plate, (3) piezo for coarse motion in x-direction, (4) tip and scanner, (5) scanner-holder (Cu prism), and (6) piezo for coarse motion in z-direction.

faster cooling are expected after optimization of the insertion pressure into Joule-Thomson stage and the ^3He - ^4He ratio of the mixture.

B. STM head and electronics

The compact and stiff STM head was designed and modeled by finite element methods for its vibrational properties in order to reduce mechanical vibration. The microscope body was made of copper and copper beryllium. These have a high hardness and a high thermal conductivity. Figure 6 shows a schematic drawing of the STM head.

A sample is fixed by molybdenum springs on a $15 \times 15 \text{ mm}^2$ square molybdenum sample plate, inserted into a sample rack made of copper beryllium at the upper part of the STM head. The STM scanner is a 6 mm piezo tube which is fixed in the scanner holder and has a maximum scan range of $2 \mu\text{m} \times 2 \mu\text{m}$ and a z-range of 200 nm at voltages of $\pm 140 \text{ V}$ and the base temperature. The STM tip is mounted in a tip holder which sits on top of the tube piezo.

The approach mechanism is based on the design by Pan.²⁸ The scanner is fixed on a hexagonal Cu prism which is clamped by six ceramic isolators glued on top of six shear-piezos. The gliding planes of the prism were made from polished sapphire. Four of the shear-piezo pieces were directly glued on the main body of the STM, while the other two are pushed by a copper beryllium spring ensuring firm mechanical contact and sufficient force between the gliding planes of the slip stick motor. The travel in z-direction is 5 mm. Further, the Cu prism is thermally anchored to the body of the STM by a thin Au wire. The advantage of using a Cu prism is its high thermal conductivity thus ensuring a constant tip temperature during scanning and a fast cooling down of only a minute after extended coarse motion. Similarly, the sample rack can glide on polished sapphire plates using six legs, each made of a ruby sphere, shear-piezo, and a ceramic isolator. Therefore, coarse motion of the sample holder in x-direction is possible (range 5 mm). A modified sample plate is used to transfer STM tips. Only by fore of the slip stick motors, the STM tip can be transferred into and out of the STM avoiding large mechanical forces on the scanner. This process is shown

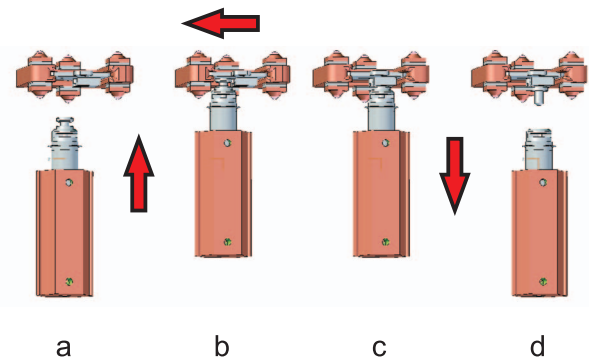


FIG. 7. (Color online) Process of tip transfer in four steps using a special sample plate and coarse motion in x and z directions.

in Fig. 7. When the tip is on the modified sample plate, it can be transferred to the preparation chamber and can undergo all surface treatments that are available also for the samples.

The high voltage electric lines to the STM are NiMn wires with a low thermal conductivity, which are thermally anchored at 4.2 K and at the ^3He cryostat. The two coaxial lines for the tunneling current and the bias voltage are anchored in the same way. These cables are of low capacitance ($\approx 30 \text{ pF/m}$) and effective damping at high frequencies (-80 dB/m at 8 GHz and a 20 dB drop per octave) to hinder infrared photon conduction and to ensure low electron temperatures at the tunneling junction.

The STM is controlled by commercial electronics²⁹ containing a PC-based real-time controller, a 22 bit multi-channel analog-to-digital/digital-to-analog converter, a high voltage power supplier, a piezo motor controller, and a scanner controller. An analog lock-in amplifier is used when performing scanning tunneling spectroscopy (STS). The STM tip and sample are connected to a commercial preamplifier³⁰ mounted outside the UHV via shielded twisted-pair cables. To avoid high-frequency noise, the STM bias voltage as well as the high voltage piezo signals are low-pass filtered with a cutoff frequency of 50 KHz.

C. Vibration isolation

The STM head is vibrationally insulated by three copper beryllium springs with resonance frequency below 1 Hz. All parts of the cryostat and the STM head were modeled with finite element methods to find their mechanical eigenmodes and frequencies. In an optimization process, the lowest eigenmodes were damped by mechanically suspension at the positions of vibration maxima or by thickening of critical parts. The UHV chambers are supported by active vibration damping systems and the pump for ^3He circulation was settled in a sound-proof case. These guarantees a z stability at STM tip of $\approx 200 \text{ fm}$.

D. 3 T superconductive magnet

A superconducting split-coil magnet was mounted around STM head to supply an out-of-plane magnetic field (see Fig. 8(a)). The coil is made of one piece of 5 km

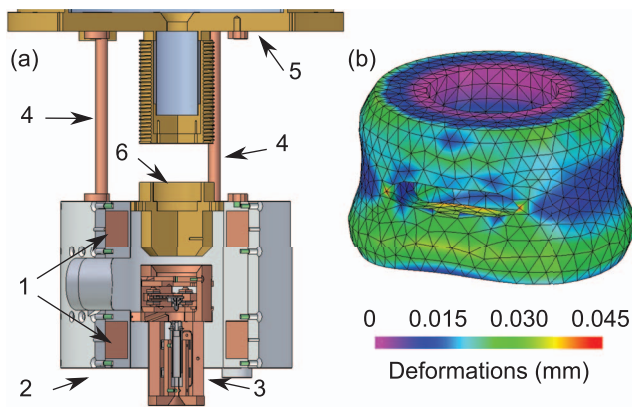


FIG. 8. (Color online) (a) Scheme of the superconducting split-coil magnet, (1) split-coil made of NbTi wire, (2) coil body, (3) STM head, (4) Cu posts as thermal anchoring between magnet and 4.2 K bath cryostat, which also support the coil body and carry the current for the coil back to ground, (5) 4.2 K bath cryostat, and (6) ^3He pot of Joule-Thomson cryostat. (b) Calculated deformations of the coil body when the coil generates a magnetic field of 3 T.

superconducting NbTi wire with a diameter of 0.2 mm, which is able to carry current of 30 A under a 5 T magnetic field. The coil was embedded into UHV compatible Epotek H77 glue for stabilization. The magnetic field and the resulting mechanical deformations of the coil were modeled using finite element methods (see Fig. 8(b)). The field distribution is shown in Fig. 9. To minimize the heat input, high-temperature superconducting wires were used to carry the current down from the liquid nitrogen bath cryostat to the superconducting coil. The coil body was made of Aluminum-6081 alloy with high thermal conductivity and high mechanical stability. It was supported and thermally anchored to 4.2 K bath cryostat by three Cu posts. To prevent electrical shorts between coil body and superconducting wire, the coil body was anodized to generate a hard and isolating Al_2O_3 surface.

The superconducting split-coil is able to generate a maximal magnetic field of 3 T at STM sample surface at currents of 30 A.

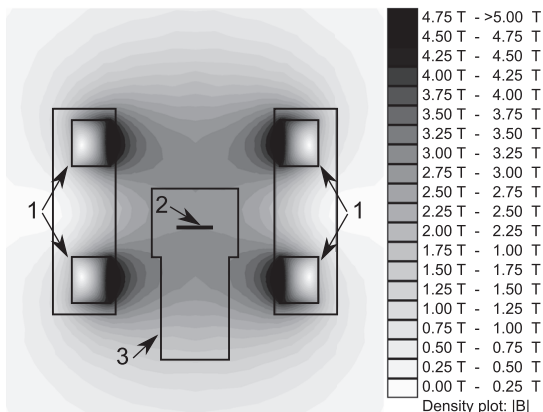


FIG. 9. Calculated field distribution inside the split-coil magnet, (1) split coils, (2) sample, and (3) STM head.

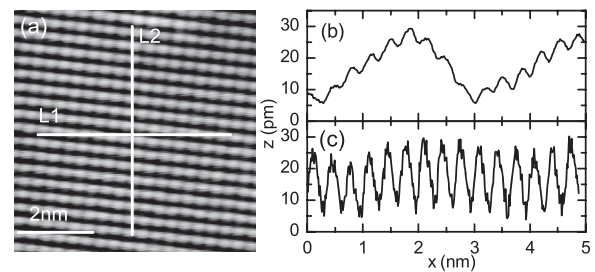


FIG. 10. Atomic resolution of Cu(100) at 930 mK. (a) Topography of Cu(100), (b) line section along L1, (c) and L2.

III. STM TEST RESULTS

In the following, we present several tests on the z stability, noise level of tunneling current, thermal drift, superconducting magnet, and energy resolution of the STM, that have been achieved in the initial testing phase of the instrument.

A. Z stability and noise level of tunneling current

An *in situ* prepared Au(111) sample was used to calibrate the scanner piezo of the STM and to check the mechanical stability. The sample surface was bombarded with Ar^+ ions and annealed at 730 K to get an atomically clean surface. High-quality STM images were obtained on this surface. The x-y calibration of the STM scanner was done by measuring the reconstructions and the z calibration was performed on atomic steps. Atomic resolution on a Cu(100) sample was achieved at 930 mK (see Fig. 10). The line section of this topography shows an in-line z-noise level of well below 500 fm and a between-lines z-noise level of below 5 pm. The main noise source in this case was the mechanical noise due to the bubbling of liquid nitrogen. It could be considerably reduced by pumping the nitrogen vapor to freeze the nitrogen or by filling the liquid nitrogen container additionally with fine copper wool. In the latter case, the high thermal conductivity of the Cu wool prevents the liquid from

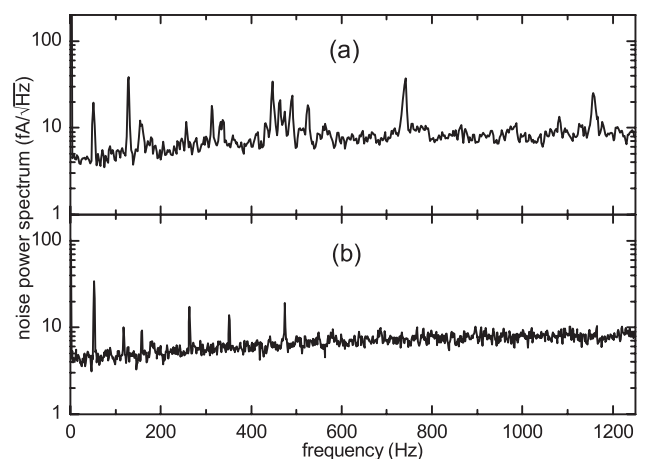


FIG. 11. Noise power spectrum of tunneling current at 1.1 K (a) with the liquid nitrogen bath fully filled and (b) with frozen nitrogen.

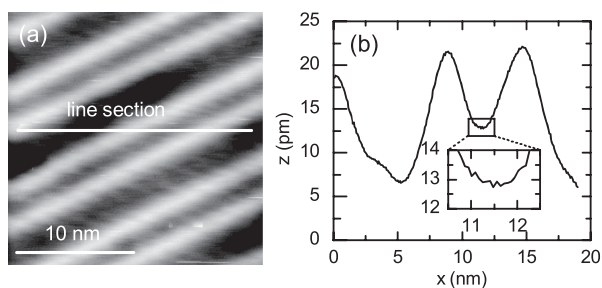


FIG. 12. (a) A topography of the herringbone reconstruction on the Au(111) surface,³¹ (b) line section of (a) which demonstrates a z-noise of about 200 fm.

boiling from the bottom of the cryostat. Instead, the liquid evaporates only near the surface. Figure 11 shows separately the noise power spectrum of the tunneling current at 1.1 K with liquid and frozen nitrogen in the cryostat. In the case of frozen nitrogen, the noise spectrum is below $6 \text{ fA}/\sqrt{\text{Hz}}$ at low frequencies which almost approaches the noise limit of the I-V converter of $4.5 \text{ fA}/\sqrt{\text{Hz}}$. A topography of the Au(111) surface (see Fig. 12) was taken at 930 mK without bubbling liquid nitrogen. Its line section demonstrates a reduced z-noise of about 200 fm.

For some studies on insulators, semiconductors, or molecules a tunneling current of several nA can damage the sample. Due to the low noise and high mechanical stability, this STM is able to investigate these fragile samples with low tunneling currents of several pA. A STM topography of the Au(111) surface with atomic resolution in constant-current mode with a tunneling current of only 1 pA and a sample bias of 1 mV is shown in Fig. 13(a). Similarly, STS measurements with low currents of $<4 \text{ pA}$ were performed on organic molecules on Au(111). An $I(U)$ curve is shown in Fig. 13(b). The $I(U)$ curve was serially recorded by ramping the bias up (solid line) and down (dashed line). The two curves are almost identical and of low noise. To perform this measurement, the feedback loop of STM controller was opened for three minutes. Therefore, any drift or vibration between tip and sample during the STS measurement should be indicated by a separation of these two $I(U)$ curves. An evaluation of the differences between the two curves of currents in combination with distance current curves allows to extract a drift

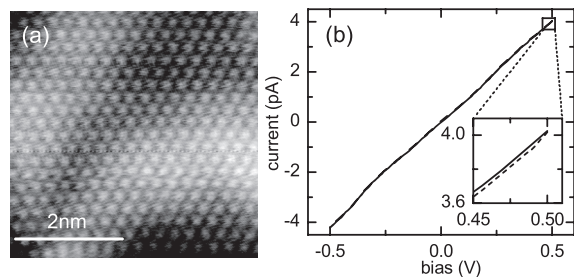


FIG. 13. (a) Topography of Au(111) recorded at 1.1 K with a tunneling current of 1 pA and a sample bias of 1 mV. (b) STS measurement with a set point of 4 pA on a organic molecule adsorbed on Au(111) ramping the voltage up (solid line) and down (dashed line).

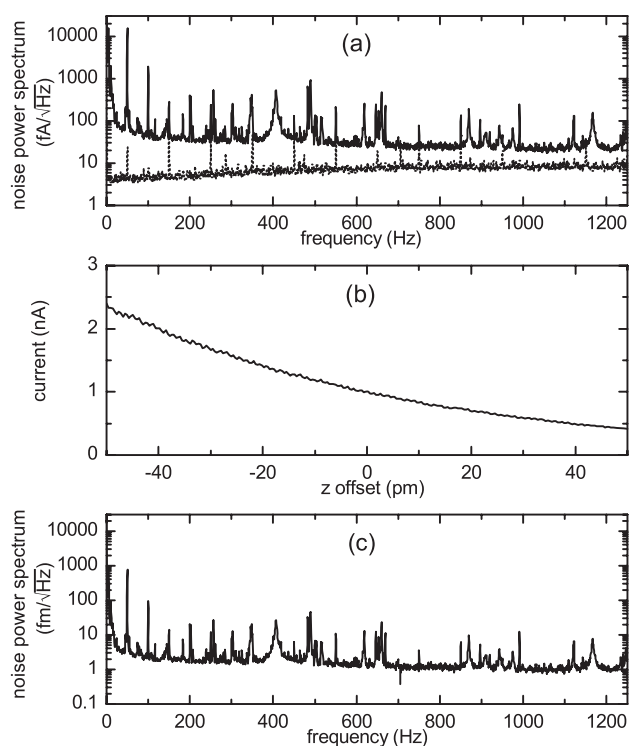


FIG. 14. (a) Current noise power of retracted tip (dashed line) and in-tunneling with turned off feedback loop (solid line). (b) Distance dependence of tunneling current $I(d)$. (c) Extracted vibration noise power.

or vibration of $<1 \text{ pm}$ from the raw data, in good agreement with the vibration level observed during scanning.

Finally, we investigate the noise due to mechanical vibrations as well as voltage fluctuations on the piezo drivers. For this, we recorded a current noise spectrum with retracted STM tip and a noise spectrum with a tip in tunneling condition but with switched off feedback loop. Figure 14(a) shows the two current noise densities. The difference in these two originates from the current of the tunneling junction being sensitive to the gap widths, bias voltage instabilities, and electronic shot noise. Using current distance curves (see Fig. 14(b)) this additional noise power can be converted in an equivalent vibration power shown in Fig. 14(c). A high stability of only $2 \text{ fm}/\sqrt{\text{Hz}}$ is achieved.

B. Lateral thermal drift

Due to the careful design of the cryostat and the STM body, the lateral thermal drift in STM measurements is negligible. Figure 15 shows four STM images of the same single Co atom on Au(111) which were taken serially at 0 min, 30 min, 100 min, and 170 min after starting injection of ^4He into Joule-Thomson stage. The temperatures of STM head and the positions of Co atom were recorded as a function of time, which demonstrated the lateral thermal drift between sample and tip. The drift during cooling STM head from 4.2 K to 1.1 K was only 0.9 nm. After the temperature became stable the lateral drift in 2 h was even smaller than

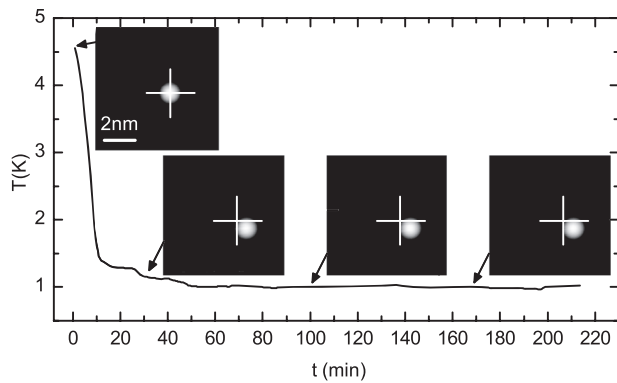


FIG. 15. STM images of the same atom demonstrating no observable lateral drift (<20 pm/h) after STM head reached at 1.1 K. The drift was only 0.9 nm when STM was cooled down from 4.5 K to 1.1 K.

the lateral resolution of STM image. This indicated that the lateral drift in the stationary situation is smaller than 20 pm/h.

C. Flux vortices in Nb(110)

To test STM operation in a magnetic field, a map of the quasiparticle density of states near the energy gap at $U = 1.2$ mV on a Nb(110) sample was performed at 1.1 K and a magnetic field of 0.21 T. The flux vortices, which are the characteristic of type II superconductors such as niobium³² were clearly resolved (see Fig. 16).

D. Energy resolution

To demonstrate the energy resolution, STS measurements on *in situ* prepared Cu(100) were performed. A superconducting Nb tip that shows a superconducting phase transition at ≈ 9.2 K was used. The Nb tip was chemically etched in a 1:1:1 admixture of HF, H₃PO₄, HNO₃ from Nb wire and was bombarded with Ar⁺ ions and annealed at ≈ 1800 K to remove the oxide. Figure 17(a) shows a dI/dV curve measured at a base temperature of 1.1 K obtained by numerical differentiation of the current with respect to the sample bias. A superconducting energy gap is clearly resolved. Using conventional BCS theory³³ the gap in the spectrum was fitted. The temperature of the Fermi functions of tip and sample was also taken into account. The resulting fit is shown in Fig. 17 as the dashed line revealing a temperature of $T_{fit} = 1.15$ K, which is close to the temperature read from the Cernox sensor on the STM head.

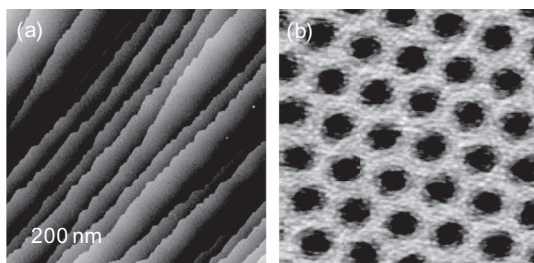


FIG. 16. (a) Topography and (b) dI^2/d^2V map of Nb(110) obtained at 1.1 K and a magnetic field of 0.21 T with a bias of $U = 1.2$ mV. The flux vortices were clearly resolved in the map of the quasiparticle density.

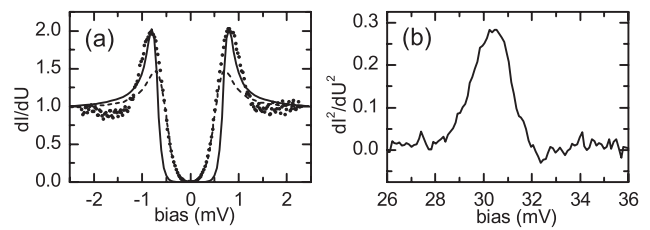


FIG. 17. (a) STS of Nb tip on Cu(100), dotted line: experimental data; dashed line: fitting curve with a fit temperature of 1.15 K reproducing the energy gap; solid line: fitting curve with a fit temperature of 650 mK reproducing the quasiparticle states. (b) Inelastic signal from the phonon excitation of CO on Au(111).

Fitting the spectrum with focus on the height of the quasiparticle peaks revealed a lower temperature of 650 mK. The real temperature of the tip and sample is in between these two extreme temperatures. This result indicates that also the electronic temperature in spectroscopic measurements is low and reveals an energy resolution that is given by the thermal limit of $3.4 kT_{fit} = 0.34$ meV for dI/dV curves and corresponding $5.4 kT_{fit} = 0.54$ meV for dI^2/d^2V curves.

Finally, the ISTS was performed on a signal CO molecule on Au(111) using a tungsten tip. An inelastic peak of phonon excitation was clearly resolved in Fig. 17(b). The peak width at half maximum is only 2 mV. This is considerably sharper than previously reported for CO on Cu(111) (Ref. 13) at similar temperatures.

IV. CONCLUSION

We have designed a compact sub-Kelvin UHV scanning tunneling microscope that combines a high energy resolution corresponding to the limit of thermal broadening at these temperatures, a high mechanical stability in combination with low current noise, magnetic fields up to 3 T and low consumption of cryogenic liquids. The design allows quick sample transfer and high sample throughput and can be operated easily.

ACKNOWLEDGMENTS

The authors thank Georg Weiß and Torben Peichl for calibrating Cernox cryogenic temperature sensors.

- ¹G. Binnig, H. Rohrer, C. Gerber, and E. Weibel, *Appl. Phys. Lett.* **40**, 178 (1982).
- ²G. Binnig, H. Rohrer, C. Gerber, and E. Weibel, *Phys. Rev. Lett.* **49**, 57 (1982).
- ³C. Chen, *Introduction to Scanning Tunneling Microscopy* (Oxford University Press, New York, 1993).
- ⁴A. L. de Lozanne, S. A. Elrod, and C. F. Quate, *Phys. Rev. Lett.* **54**, 2433 (1985).
- ⁵A. P. Fein, J. R. Kirtley, and R. M. Feenstra, *Rev. Sci. Instrum.* **58**, 1806 (1987).
- ⁶D. M. Eigler and E. K. Schweizer, *Nature (London)* **344**, 524 (1990).
- ⁷P. Davidsson, H. Olin, M. Persson, and S. Pehrson, *Ultramicroscopy* **42–44**, 1470 (1992).
- ⁸S. H. Tessmer, D. J. V. Harlingen, and J. W. Lyding, *Rev. Sci. Instrum.* **65**, 2855 (1994).
- ⁹J. W. G. Wildöer, A. J. A. van Roy, H. van Kempen, and C. J. P. M. Harmans, *Rev. Sci. Instrum.* **65**, 2849 (1994).

- ¹⁰S. H. Pan, E. W. Hudson, and J. C. Davis, *Rev. Sci. Instrum.* **70**, 1459 (1999).
- ¹¹Y. J. Song, A. F. Otte, V. Shvarts, Z. Zhao, Y. Kuk, S. R. Blankenship, A. Band, F. M. Hess, and J. A. Stroscio, *Rev. Sci. Instrum.* **81**, 121101 (2010).
- ¹²J. A. Stroscio and D. M. Eigler, *Science* **254**, 1319 (1991).
- ¹³A. J. Heinrich, C. P. Lutz, J. A. Gupta, and D. M. Eigler, *Science* **298**, 1381 (2002).
- ¹⁴L. Gerhard, T. K. Yamada, T. Balashov, A. F. Takács, R. J. H. Wesselink, M. Däne, M. Fechner, S. Ostanin, A. Ernst, I. Mertig, and W. Wulfhekel, *Nat. Nanotechnol.* **5**, 792 (2010).
- ¹⁵RHK Technology, USA.
- ¹⁶Omicron NanoTechnology GmbH, Germany.
- ¹⁷Unisoku Co., Ltd, Japan.
- ¹⁸J. Klein, A. Léger, M. Belin, D. Défourneau, and M. J. L. Sangster, *Phys. Rev. B* **7**, 2336 (1973).
- ¹⁹T. Balashov, A. F. Takács, W. Wulfhekel, and J. Kirschner, *Phys. Rev. Lett.* **97**, 287201 (2006).
- ²⁰T. Balashov, T. Schuh, A. F. Takacs, A. Ernst, S. Ostanin, J. Henk, I. Mertig, P. Bruno, T. Miyamachi, S. Suga, and W. Wulfhekel, *Phys. Rev. Lett.* **102**, 257203 (2009).
- ²¹T. Schuh, T. Balashov, T. Miyamachi, A. F. Takacs, S. Suga, and W. Wulfhekel, *J. Appl. Phys.* **107**, 9E156 (2010).
- ²²U. Schlickum, W. Wulfhekel, and J. Kirschner, *Appl. Phys. Lett.* **83**, 2016 (2003).
- ²³F. Pobell, *Matter and Methods at Low Temperatures* (Springer-Verlag, Berlin, 1996).
- ²⁴J. W. Ekin, *Experimental Techniques for Low-Temperature Measurements* (Oxford University Press, New York, 2006).
- ²⁵Lake Shore Cryotronics, USA.
- ²⁶F. G. Brickwedde and U. S. N. B. of Standards., *The "1958 He⁴ Scale of Temperatures"* (Washington, 1960).
- ²⁷C. F. Barenghi, R. J. Donnelly, and R. N. Hills, *J. Low Temp. Phys.* **51**, 319 (1982).
- ²⁸S. H. Pan, Piezo-electric Motor, International Patent Publication No. WO 93/19494, International Bureau, World Intellectual Property Organization (30 September 1993).
- ²⁹Nanonis Control System, SPECS Surface Nano Analysis GmbH, Germany, see www.specs.com.
- ³⁰Variable Gain Low Noise Current Amplifier DLPCA-200, FEMTO Messtechnik GmbH, Germany.
- ³¹J. V. Barth, H. Brune, G. Ertl, and R. J. Behm, *Phys. Rev. B* **42**, 9307 (1990).
- ³²A. A. Abrikosov, *Z. Eksp. Teor. Fiz.* **32**, 1442 (1957).
- ³³M. Tinkham, *Introduction to Superconductivity*, 2nd ed. (McGraw-Hill, New York, 1996).